# Stable Orbiting around Small Moons using the $J_2$-perturbed Elliptic Restricted Problem

Hongru Chen*
*Kyushu University, Fukuoka, 8190367, Japan*

Xiyun Hou†
*Nanjing University, Nanjing, 210023, China*

Mai Bando‡
*Kyushu University, Fukuoka, 8190367, Japan*

**Confirmed small-body missions MMX and HERA are set to explore Martian moons and the binary asteroid Didymos' moon Dimorphos, respectively. Orbital dynamics around these small moons differ substantially from those around previously visited targets. Simplified models, such as the circular-restricted three-body problem, cannot yield accurate predictions for orbits and their stability in real-world operations. To be specific, the orbit of the small moon and its vicinity are significantly perturbed by the oblateness of the planet and their relative positions. Realistic control constraints and the unstable 3:1 resonance of retrograde orbits further complicate orbit maintenance around a small moon. Therefore, minimizing the dynamical perturbation on baseline orbits resulting from model mismatches is crucial. This paper introduces the "J2-ER3BP+GH" model dedicated to describing the orbital dynamics around the small moon. It incorporates the $J_2$ perturbation of the planet on the elliptic-restricted three-body problem and can accommodate a non-spherical gravity field of the moon. Bounded orbits can still be identified without much effort in this sophisticated model. Baseline orbits around Phobos and Dimorphos from the J2-ER3BP+GH become much easier to maintain, as verified in the high-fidelity dynamic and control environments.**

## Nomenclature

| | | |
|---|---|---|
| $\Xi, H, Z$ | = | coordinates along the three axes of the inertial frame |
| $x, y, z$ | = | coordinates along the three axes of the rotating frame |
| $A_x, A_y, A_z$ | = | amplitudes of an orbit along the axes of the rotating frame |
| $m_1, m_2, m_3$ | = | masses of the planet, moon, and spacecraft, respectively |

*Assistant Professor, Department of Aeronautics and Astronautics; Corresponding author: hongru.chen@hotmail.com
†Professor, School of Astronomy and Space Science
‡Professor, Department of Aeronautics and Astronautics

| | | |
|---|---|---|
| $r_1, r_2$ | = | distances from the primary and the secondary, respectively |
| $f$ | = | true anomaly of the orbit of the primary system (or the "primary orbit") |
| $\omega$ | = | argument of periapsis of the primary orbit |
| $u$ | = | $\omega + f$ ; argument of true latitude |
| $t$ | = | time |
| $TU$ | = | time unit |
| $LU$ | = | length unit |
| $\mathcal{U}, U$ | = | gravitational potential in the unnormalized and normalized coordinate systems, respectively |
| $J_l$ | = | $l$-th-degree zonal term of a gravity harmonics model |
| $C_{l,m}, S_{l,m}$ | = | $l$-th-degree and $m$-th-order Stroke coefficients of a gravity harmonics model |
| $\bar{R}$ | = | reference radius of a celestial body |
| $A_2$ | = | an adapted form of the planet's $J_2$ term; see Eq. 6 |
| $e$ | = | eccentricity of the primary orbit |
| $a$ | = | osculating semi-major axis of the primary orbit |
| $n$ | = | mean motion of the primary orbit |
| $\bar{a}, \bar{n}$ | = | mean semi-major axis and mean motion under $J_2$ |
| $D$ | = | Distance between two primaries |
| $\dot{(\cdot)}, \ddot{(\cdot)}$ | = | first and second derivatives with respect to time |
| $(\cdot)', (\cdot)''$ | = | first and second derivatives with respect to $u$ |
| $\mu$ | = | ratio of the mass of the moon to the total |
| $c, k_1, k_2$ | = | coefficient functions of $J_2$ and $f$ in the $J_2$-perturbed elliptic-restricted 3-body problem |
| $\mathbf{\Omega}$ | = | pseudo-potential of the $J_2$-perturbed circular-restricted 3-body problem |
| $C$ | = | Jacobi constant of the $J_2$-perturbed circular-restricted 3-body problem |
| $\xi$ | = | $e \cos f$; introduced new state |
| $\boldsymbol{E}$ | = | extended state vector |
| $\mathbf{F}$ | = | Jacobian matrix of the extended system |
| $\mathbf{A}, \mathbf{B}, \mathbf{C}$ | = | submatrices of Jacobian matrix |
| $\mathbf{\Phi}$ | = | state transition matrix |
| $\boldsymbol{\nu}$ | = | eigenvector of the monodromy matrix |
| $\Delta v$ | = | velocity increment |
| Subscripts | | |
| 0 | = | initial epoch |

| | | |
|---|---|---|
| p | = | planet |
| m | = | moon |
| Acronyms | | |
| CR3BP | = | circular-restricted 3-body problem |
| ER3BP | = | elliptic-restricted 3-body problem |
| CR3BP+GH | = | CR3BP plus moon's non-spherical gravity model |
| ER3BP+GH | = | ER3BP plus moon's non-spherical gravity model |
| J2-CR3BP+JM | = | planet's $J_2$-perturbed CR3BP plus moon's zonal gravity model |
| J2-CR3BP+GH | = | planet's $J_2$-perturbed CR3BP plus moon's non-spherical gravity model |
| J2-ER3BP+GH | = | planet's $J_2$-perturbed ER3BP plus moon's non-spherical gravity model |
| HF | = | high-fidelity |
| PO | = | periodic orbit |
| QPO | = | quasi-periodic orbit |

# I. Introduction

Small bodies, such as asteroids, comets, and small planetary moons, are of great scientific interest as they preserve pristine relics that are clues to the formation of the early solar system. Additionally, small bodies are believed to be rich in water and rare metals. These resources can be utilized to power space activities and bases. On the other hand, some small bodies pose constant and potentially fatal threats to the Earth as they regularly approach our planet. Knowledge of the interior structures of small bodies can guide the strategy of planetary defense. Missions such as Hayabusa-1 and -2, Rosetta, and Osiris-REx have returned valuable information about small bodies. The confirmed MMX [1, 2] and HERA [3, 4] with its CubeSat payloads Milani [5, 6] and Juventas [7] will be launched in 2024 to explore and land on the Martian moon Phobos and the binary asteroid's moon Dimorphos, respectively. However, the orbital dynamics around these small moons are very different from those around the previously visited targets (i.e., heliocentric planets and asteroids, and large planetary moons).

For small-body missions, robust proximity orbiting is highly desirable for the following engineering and scientific outcomes: a) long-term orbiting provides abundant ballistic arcs contributing to rapid and accurate orbit determination and geodesy (i.e., to recover gravity coefficients, libration amplitude, etc) [8]; b) low-altitude orbiting constrains impact velocity, derisking landing operations; and c) if high-latitude orbiting can also be realized, that will enhance global mapping and geodesy, and facilitate polar landing. However, pre-studies for the MMX mission experienced large difficulty in maintaining a quasi-satellite orbit (QSO) around Phobos, which is broadly linearly stable, compared to maintaining an Earth-Moon halo orbit, which is typically linearly unstable (private communication with JAXA project

teams). This counter-intuitive result can be attributed to the fast orbital dynamics, the unstable resonance intersecting the QSO families, which will be further explained in Sec. II, and significant dynamical perturbations not considered in the orbit design stage.

Robust orbiting operations require certain stability of the baseline orbit and stationkeeping control. Baseline orbits are not directly found in the high-fidelity model but are typically identified in a simplified model, such as the two-body problem and the circular-restricted 3-body problem (CR3BP). Insights into the simplified models are clear, and periodic orbits can be easily identified. However, if the simplified model for orbit design (hereafter referred to as the "substitute model") does not accurately reflect the realistic dynamical environment, the designed orbit, even though stable in the substitute model, will experience significant dynamical perturbation and diverge quickly in the real world. Consequently, frequent controls will be necessary to compel the truth trajectory to follow the unrealistic baseline orbit. However, in the early phases of a proximity mission, stationkeeping relies on ground-based orbit determination (OD), and the control interval (or coast duration) typically spans a couple of days. The coast duration is necessary for the OD team to collect sufficient tracking data for delivering an orbit accuracy permissible for the following orbit control ([9, 10]). Therefore, if the orbit cannot stay bounded in the presence of dynamical perturbation and OD errors during the cost duration, stationkeeping is likely to fail. While efforts to enhance OD operations for reducing OD errors are essential, enhancing the substitute model's accuracy is equally crucial in mitigating perturbations on the baseline orbit, contributing to successful stationkeeping. Moreover, the substitute model with improved accuracy should still facilitate a straightforward identification of bounded baseline orbits.

There have been efforts to improve the accuracy of substitute models. For instance, high-degree gravity terms of the non-spherical moon can be added to the CR3BP and periodic orbit can be computed in the new models [11, 12]. However, those models did not consider the high-degree gravity terms of the planet. Given the small gravity of a small moon and the close distance to its planet, the 2nd-degree gravity term (i.e., $J_2$) of the planet also poses a significant influence on the orbit and the vicinity of the small moon. Unlike the high-degree gravity terms of the moon, the high-degree gravity terms of the planet cannot be directly added to the CR3BP or the elliptic-restricted 3-body problems (ER3BP) [13] without accounting for its perturbation on the primary orbit. Some studies have incorporated the perturbation from the oblateness (or the $J_2$ term) of the planet in the CR3BP [14, 15]. Nevertheless, our experiments with the Mars' $J_2$-perturbed CR3BP do not result in noticeable differences in orbital profiles or stability compared to those obtained into the CR3BP. To be more accurate, it is the elliptic orbital motion of the primary system perturbed by the oblateness of the planet that exerts constant and significant perturbation on orbits around the moon. Additionally, as reasoned in the preceding paragraph, whether an orbit from the substitute model is operational should be verified in the high-fidelity environment. There is no evidence to suggest that orbits from any of the aforementioned models are sufficiently true in the high-fidelity model to enable robust orbiting around the small moon. The mean $J_2$-perturbed elliptic orbit described by Kozai [16] was used to approximate the Mars-Phobos system [17], and the ephemeris

model based on it yielded accurate predictions for spacecraft orbits when compared to those propagated in the true full-ephemeris model [18, 19]. A substitute model based on Ref. [16] should reveal operational baseline orbits.

The present paper develops the $J_2$-perturbed elliptic-restricted 3-body problem, wherein the motion of the moon is governed by the planet's $J_2$-perturbed elliptic 2-body problem [16]. Since the gravity field of the moon does not perturb its orbit but can influence the motion of spacecraft, a precise non-spherical gravity model of the moon can be directly added to this model (see Sec. III). This proposed model is set up in the rotating frame and termed "J2-ER3BP+GH". While this model contains many factors, all significant in the vicinity of a small moon, it permits a straightforward identification of bounded baseline orbits (i.e., periodic and quasi-periodic orbits). The approach to computing bounded orbits is explained in Sec. IV. The model validity and the effective stability of the orbits from the J2-ER3BP+GH and other substitute models (e.g., ER3BP and ER3BP+GH) should be examined and compared. This evaluation is conducted through high-fidelity simulations that demonstrate the orbiting behavior around Phobos and Dimorphos (see Sec. V). Conclusions are given in the final section.

## II. Problem statement: unstable orbital environment around small moons

For a small moon close to its planet, its vicinity is significantly influenced by the gravity of the planet, and its sphere of influence is confined to a small radius. The high-degree gravity terms of the planet also exert significant influences on the orbit and the vicinity of the small moon. Therefore, the spacecraft's orbit around a small moon is also influenced by the non-spherical gravity field of the planet as well as by the relative position (or ephemeris) of the two primary bodies. The designed baseline orbit that does not account for such dynamical perturbation cannot be easily maintained. If the ephemeris of the primaries is not accurate, this error may not translate into obvious errors in the spacecraft's orbit around the moon, but can significantly disturb OD and geodesy operations. A small-moon mission, such as the MMX and HERA, will encounter these emerging issues. Concerning the issue resulting from the ephemeris error, previous work has briefly touched on the mitigation of its impacts on OD and geodesy [8]. The objective of the present paper is to reveal effectively stable orbits in the unique dynamical environment around the small moon.

To orbit around a small moon, bounded orbits held by the gravity of both primary bodies are options for the baseline orbit in the sense of relative motion. The planar 1:1 quasi-satellite orbit (QSO) identified in the CR3BP, which is retrograde and linearly stable, has been intensively studied [20–23] and suggested for Martian moons exploration [24]. However, the elliptic motion of the primary system and the non-spherical gravity field of the primaries constantly perturb the baseline orbit from the simplified CR3BP. Related to the short orbital period of the small moon, one revolution of the spacecraft orbit around the moon is also short, roughly 6 hours for a QSO about Phobos and 10 hours for a QSO around Dimorphos. Accumulated perturbation can have destroyed the bounded motion before the stationkeeping control can take place. Note that deep-space stationkeeping controls relying on the ground-based OD cannot be implemented frequently; instead, it requires an interval of 5 to 7 days for achieving permissible OD accuracy [9, 10]. Figure 1 shows

a periodic QSO, whose size is $29 \times 46$ [km] (i.e., $A_x \times A_y$, where $A_x$ is the orbit amplitude along the $x$-axis, or the planet to moon direction, and $A_y$ the amplitude along the $y$-axis in the rotating frame), obtained in the Mars-Phobos CR3BP, and the trajectory propagated from the converted initial state in the high-fidelity (HF) model with arbitrary initial phases $f_0$ of the primary system. In the HF model, the trajectory quickly departs from its nominal periodic orbit (PO), even in the absence of OD errors.

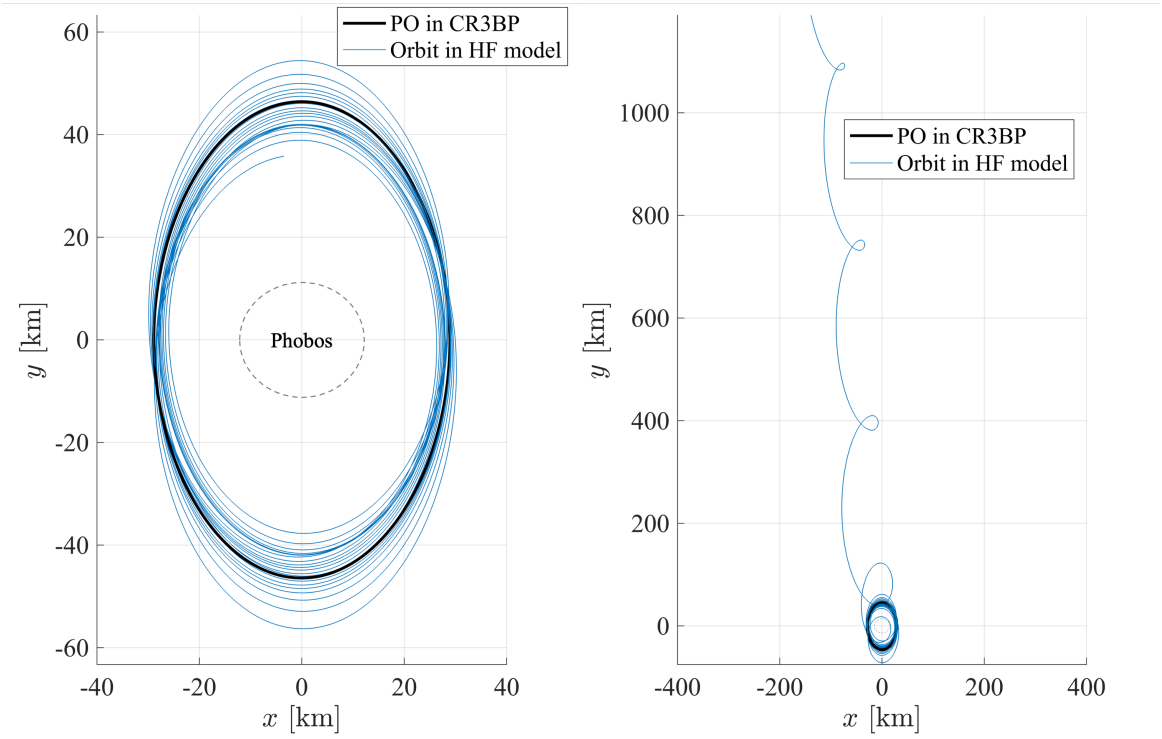


(a) $f_0 = -125°$ (b) $f_0 = 150°$

**Fig. 1 A QSO obtained in the CR3BP and its evolution in the high-fidelity model for 5 days.**

Apart from the dynamical perturbation experienced in the real world, the orbit in the CR3BP may not be as stable as its linear stability indicates. For better global mapping and geodesy, previous work [19] has computed families of periodic 3-dimensional QSO (3DQSO) around Phobos in the CR3BP. The $x$-amplitude $A_x$ and out-of-plane amplitude $A_z$ of the 3DQSO belonging to different resonant families are displayed in Fig. 2. The annotated resonance, $m : n$, represents the ratio of the vertical to the horizontal revolutions. The color scale of Fig. 2a indicates the linear stability, which is the normalized maximum eigenvalue of the monodromy matrix of each orbit. If the linear stability equals 1, the orbit is linearly stable. Despite the wide linear-stability region, it is found challenging to maintain a low-altitude linearly-stable QSO around Phobos under operational errors. Figure 2b presents the more accurate stability situation. The color scale indicates the ratios of bounded orbits from the Monte Carlo simulation: 1000 runs of one-week propagation in the CR3BP for each orbit whose initial condition is perturbed by random OD errors (i.e., $1\sigma$ 3.4 cm/s

and 50 m on each component were used). The difference between Fig. 2a and Fig. 2b is mainly the instability band appearing inside the linear-stability region. This instability band stretches from $[A_x, A_z] = [29, 0]$ [km] to higher $A_z$ and smaller $A_x$. Hénon [25], Bernest [21], and Lam and Whiffen [26] have noted that the stability domain of a planar QSO is constrained by the planar unstable period-3 orbit. In other words, at the intersection of the planar 1:1 family and the period-3 family, where the arguments of a pair of conjugate eigenvalues of the monodromy matrix are ±120°, the stability domain of the QSO is close to zero, despite the linear stability it presents. The eigenvalues of the monodromy matrix of the unstable 3DQSOs inside the linear-stability region also exhibit intersections with the 3:1 resonance, as annotated in Fig. 2b.

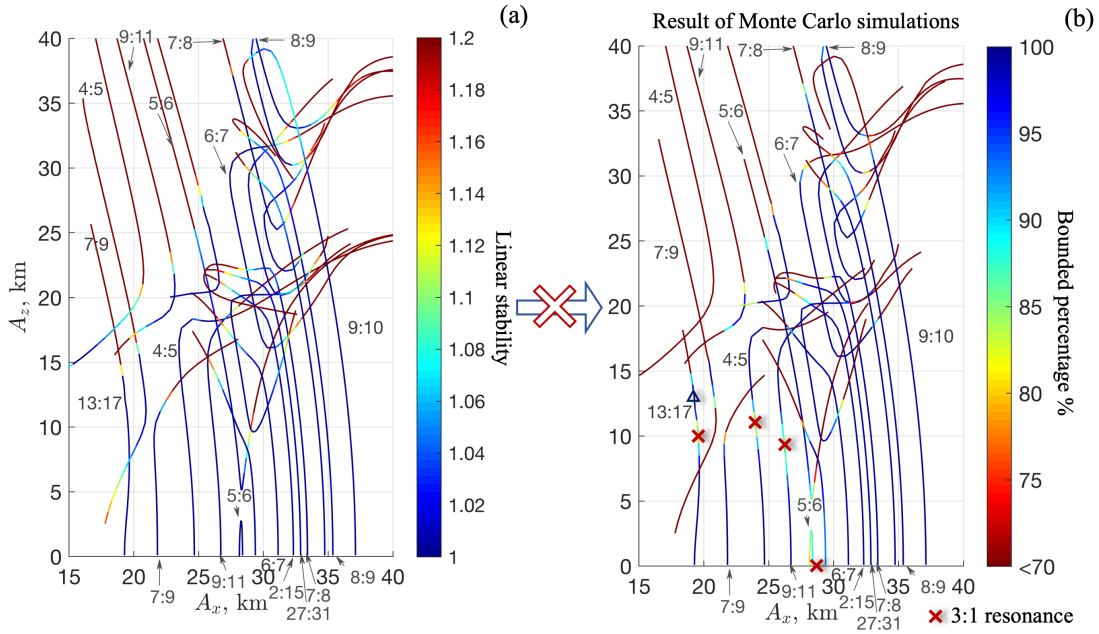


Adapted with permission from Chen, H., Canalias, E., Hestroffer, D., and Hou, X., "Effective Stability of Quasi-Satellite Orbits in the Spatial Problem for Phobos Exploration," *Journal of Guidance, Control, and Dynamics*, Vol. 43, No. 12, 2020, pp. 2309–2320. Copyright © 2020 by Hongru Chen.

**Fig. 2 Linear stability and effective stability of families of 3DQSO around Phobos [19].**

The Poincaré-map analysis, another form of dispersion analysis, is performed. For an examined orbit, its initial state is perturbed while its Jacobi constant is maintained, and propagated in the CR3BP. The Poincaré section is set at $y = 0$, where the divergent pattern is distinct, and on the $v_x < 0$ side. Fig. 3 shows the Poincaré maps for the unstable QSO (i.e., intersecting the 3:1 resonance) and a stable QSO (marked by the blue triangle in Fig. 2b) from the 13:17 family. The diverging traces of the unstable QSO resemble the unstable manifold of a period-3 orbit. By contrast, states propagated from the displaced initial conditions of the stable QSO stay around the states propagated from the initial. The Poincaré maps also reveal the confined stability domain of retrograde orbits.

## III. Dynamic Models

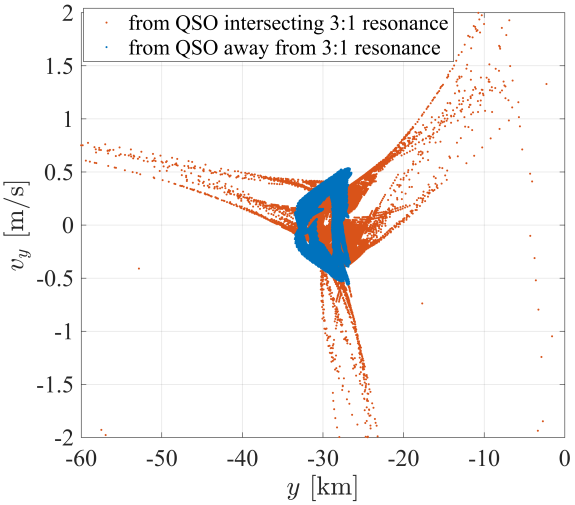


**Fig. 3 Poincaré dispersion maps for the QSOs intersecting and away from the 3:1 resonance.**

### A. Mean $J_2$-perturbed elliptic model

The non-spherical gravity field of the planet can shift the moon's orbit from what is predicted by the two-body problem, and in turn, influence the motion of the spacecraft relative to the moon. Perturbations can manifest as mean, long-periodic, and short-periodic effects [27]. The mean $J_2$-perturbed elliptic orbit described by Kozai [16] was adopted to describe the Mars-Phobos system [17]. It is assumed that the orbital plane and equatorial planes of the bodies are co-planar. The apsis of the moon's orbit precesses at $\dot{\omega}$ due to the $J_2$ perturbation of the planet. This mean $J_2$-perturbed elliptic two-body problem can be referred to as the "J2-Elliptic" model for simplicity.

The gravity of a small moon does not significantly perturb the J2-Elliptic model. However, in describing spacecraft orbits, the high-degree gravity harmonic (GH) terms of the moon are also influential and should be considered. In computing the moon's non-spherical gravity forces on the spacecraft, the principal axis of the moon is assumed to be constantly pointing to the center of mass of the planet, representing a tidal lock situation. The described model governing the spacecraft's orbital motion is depicted in Fig. 4. The spacecraft orbits generated in this dynamic model closely matched those obtained from the true full-ephemeris model [18, 19]. This result suggests the necessity of considering the planet's gravity up to the 2nd degree and the eccentricity of the moon's orbit, concerning orbiting around a small moon. However, the J2-Elliptic model is a simplified ephemeris model useful for quick simulation and verification. Bounded orbits cannot be easily identified in it. In the following section, it is adapted into the $J_2$-perturbed restricted three-body problems for the purpose of orbit design.

### B. $J_2$-perturbed elliptic-restricted three-body problem

In the restricted three-body problem, a particle or spacecraft $m_3$ moves in a dynamical environment dominated by two primary bodies $m_1$ and $m_2$ orbiting about each other, where $m_1 > m_2 \gg m_3$. The motion of the spacecraft can be

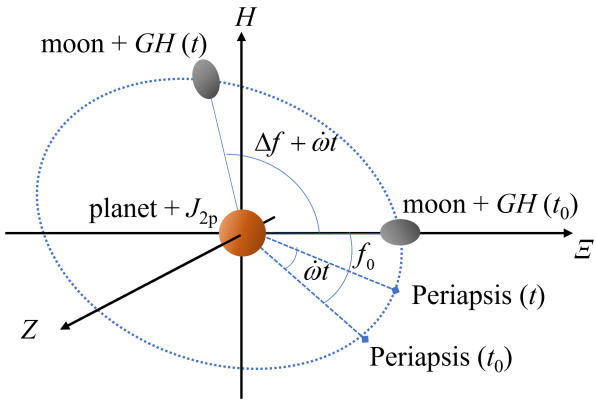


**Fig. 4 Schematic of the dynamical environment influenced by the planet's $J_2$-perturbed elliptic system and the moon's non-spherical gravity.**

described in the rotating frame, where the $x$-axis is aligned with the $m_1$ to $m_2$ directions, the $z$-axis is normal to the primary orbit, and the $y$-axis completes the right-hand coordinate system. The primaries are separated by $D$, which varies with time unless the problem is circular.

As reasoned in previous sections, it is essential to consider the gravity of the planet up to the $J_2$ term for spacecraft orbits around a small moon. As the high-degree gravity terms of the small moon do not significantly influence its orbit around the planet but can influence spacecraft's orbits around it, a non-spherical gravity model of the moon can be directly added to the substitute model. In computing the force of the moon acting on the spacecraft, the model assumes a tidal lock situation, where the equatorial planes are aligned with the orbital plane of the primary system, and the principal axis of the moon is pointed to the center of the planet. While tidal locks are common among many discovered planetary moons, including Martian moons and many binary moons, this model cannot be directly used in scenarios around non-tidally locked moons.

Like the general restricted three-body problem, this model is set up in the rotating frame. Additionally, as the focus is the spacecraft's orbit around the small moon, unlike the general restricted three-body problem, the coordinate origin is placed on the center of mass of the moon. The intention of this setting is to avoid the error at the conversion to the HF full-ephemeris model due to the mismatch between the modeled ephemeris (i.e., the mean $J_2$-perturbed orbit) and the true ephemeris (i.e., the moon's orbit under the influence of planet's full gravity model). The schematic of the dynamic and coordinate systems is presented in Fig. 5. Equations of motion of the spacecraft in this moon-centered pulsating

rotating frame are written as,

$$\ddot{x} - 2\dot{u}\dot{y} - \ddot{u}y - \dot{u}^2 x = \frac{\partial \mathcal{U}}{\partial x} + \frac{Gm_1}{D^2}\left(1 + \frac{A_2}{D^2}\right) \tag{1}$$

$$\ddot{y} + 2\dot{u}\dot{x} + \ddot{u}x - \dot{u}^2 y = \frac{\partial \mathcal{U}}{\partial y} \tag{2}$$

$$\ddot{z} = \frac{\partial \mathcal{U}}{\partial z} \tag{3}$$

where the argument of true latitude $u$ represents the angular difference of the rotating frame from the inertial reference, and is the sum of the argument of periapsis and the true anomaly of the primary orbit, expressed as

$$u = \omega + f \tag{4}$$

The gravitational potential $\mathcal{U}$ is expressed as

$$\begin{aligned}\mathcal{U} = &\frac{Gm_1}{r_1}\left\{1 - \frac{A_2}{r_1^2}\left[\left(\frac{z}{r_1}\right)^2 - \frac{1}{3}\right]\right\} + \frac{Gm_2}{r_2}\left\{1 - \sum_{l=2}^{\infty} J_{l\mathrm{m}}\left(\frac{\bar{R}_m}{r_2}\right)^l P_l\left[\sin(\phi_{\mathrm{sc}})\right]\right\} \\ &+ \frac{Gm_2}{r_2}\left\{\sum_{l=2}^{\infty}\sum_{m=1}^{l}\left(\frac{\bar{R}_m}{r_2}\right)^l P_{l,m}\left[\sin(\phi_{\mathrm{sc}})\right]\left[C_{l,m}\cos(m\lambda_{\mathrm{sc}}) + S_{l,m}\cos(m\lambda_{\mathrm{sc}})\right]\right\}\end{aligned} \tag{5}$$

where $A_2$ represents the $J_2$ term of the planet expressed as,

$$A_2 = \frac{3J_{2\mathrm{p}}\bar{R}_{\mathrm{p}}^2}{2} \tag{6}$$

and $r_1$ and $r_2$ represent the distance of the spacecraft from the planet and the moon, respectively. Subscripts "p" and "m" are used to indicate the planet and the moon separately. $\bar{R}$ and $J_l$ are the reference radius and the $l$-th zonal harmonics coefficient of the celestial body, respectively. $C_{l,m}$ and $S_{l,m}$ represent the $l$-th degree $m$-th order coefficients of the moon, corresponding to tesseral and sectional terms. $P_{l,m}$ represents the $l$-th degree $m$-th order Legendre polynomials. Angles $\phi_{\mathrm{sc}}$ and $\lambda_{\mathrm{sc}}$ represent the geocentric latitude and longitude of the spacecraft with respect to the moon, respectively. Because the center is at the moon, the force of the planet acting on the moon should be subtracted as the right-hand side of Eq. (1) presents.

The mean semi-major axis $\bar{a}$ and mean motion $\bar{n}$ of the $J_2$-perturbed primary orbit are expressed as [16],

$$\bar{a} = a\left(1 - \frac{A_2}{a^2(1-e^2)^{3/2}}\right) \tag{7}$$

$$\bar{n} = n\left(1 + \frac{A_2}{a^2(1-e^2)^{3/2}}\right) \tag{8}$$

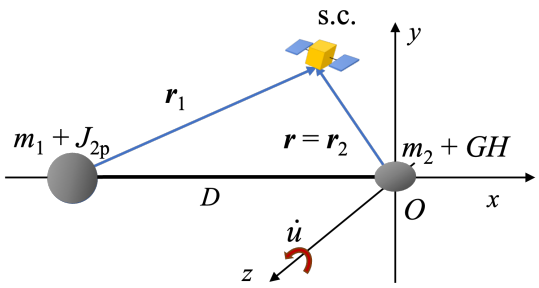


**Fig. 5 Schematic of the dynamical environment and pulsating rotating frame of the $J_2$-perturbed restricted three-body problem.**

where $e$ is the eccentricity of the primary orbit, and the osculating $a$ and $n$ satisfy,

$$a^3 n^2 = G(m_1 + m_2) \tag{9}$$

The distance between the primary bodies is approximated by the mean distance depending on the phase $f$ of the primary orbit, expressed as,

$$D(f) = \frac{\bar{a}(1-e^2)}{1+e\cos f} = a\left(\frac{1-e^2}{1+e\cos f} - \frac{A_2}{a^2\sqrt{1-e^2}(1+e\cos f)}\right) = ac_1 \tag{10}$$

Regarding the angular rate $\dot{u}$ of the rotating frame, we first derive the time derivative of the true anomaly of the primary orbit, which is expressed as,

$$\dot{f} = \frac{\bar{n}\bar{a}\bar{b}}{D^2} = \frac{\bar{n}\bar{a}^2\sqrt{1-e^2}}{D^2} = \frac{\bar{n}(1+e\cos f)^2}{(1-e^2)^{3/2}} = \frac{n[a^2(1-e^2)^{3/2}+A_2](1+e\cos f)^2}{a^2(1-e^2)^3} \tag{11}$$

where $\bar{b}$ denotes the mean semi-minor axis. Under the $J_2$ perturbation, the drift rate of the argument of periapsis is given by,

$$\dot{\omega} = \frac{nA_2}{a^2(1-e^2)^2} \tag{12}$$

Then, the angular rate of the rotating frame with respect to the inertial space is expressed as

$$\dot{u} = \dot{f} + \dot{\omega} = n\left(\frac{[a^2(1-e^2)^{3/2}+A_2](1+e\cos f)^2 + A_2(1-e^2)}{a^2(1-e^2)^3}\right) = nc_2 \tag{13}$$

Because $\dot{\omega}$ is assumed constant under the mean $J_2$ perturbation,

$$\ddot{u} = \ddot{f} \tag{14}$$

where

$$\ddot{f} = -\frac{2\bar{n}(1+e\cos f)e\sin f}{(1-e^2)^{3/2}}\dot{f} = -\frac{2e\sin f}{1+e\cos f}\dot{f}^2 \tag{15}$$

Equations (7)-(15) can be substituted into Eq. (1)-(3). When expanding Eq. (1)-(3), one can find that the system essentially depends on $f$ of the primary system. In the ER3BP, the true anomaly is preferred as an independent variable over time. However, in the $J_2$-perturbed problem, the coordinate system is rotating at $\dot{u}$ instead of $\dot{f}$ with respect to the inertial space. Hence, $u$ is chosen to be the independent variable. The time unit $TU$ becomes $1/\dot{u}$ (i.e., $dt/du$). Because $u$ and $f$ do not vary at the same pace, $f$ should be obtained by integrating its derivative $f'$ with respect to $u$. According to Eq. (13) and Eq. (11), $f'$ is given by,

$$f'(f) = \frac{df}{du} = \frac{\dot{f}}{\dot{u}} = \frac{[a^2(1-e^2)^{3/2}+A_2](1+e\cos f)^2}{[a^2(1-e^2)^{3/2}+A_2](1+e\cos f)^2 + A_2(1-e^2)} \tag{16}$$

We can also normalize the length of the system by setting the length unit $LU = D$. As a result, the distance between the two primaries becomes one. The normalized coordinates can be denoted by another set of denotations. For simplicity, without causing much confusion, the same denotations are adopted for the normalized coordinates hereafter. Equations of motion Eq.(1)-(3) with respect to the independent variable $u$, expressed in the normalized coordinates are,

$$x'' - 2y' - k_1 y + k_1 x' + (k_2 - 1)\,x = \frac{1}{c}\left[\frac{\partial U}{\partial x} + (1-\mu)\left(1+\frac{A_2}{D^2}\right)\right] \tag{17}$$

$$y'' + 2x' + k_1 x + k_1 y' + (k_2 - 1)\,y = \frac{1}{c}\frac{\partial U}{\partial y} \tag{18}$$

$$z'' + k_1 z' + k_2 z = \frac{1}{c}\frac{\partial U}{\partial z} \tag{19}$$

where $(\cdot)'$ and $(\cdot)''$ represent the first and second derivatives with respect to $u$, respectively, and

$$\begin{aligned} U = {} & \frac{(1-\mu)}{r_1}\left\{1 - \frac{A_2}{D^2 r_1^2}\left[\left(\frac{z}{r_1}\right)^2 - \frac{1}{3}\right]\right\} + \frac{\mu}{r_2}\left\{1 - \sum_{l=2}^{\infty} J_{l\mathrm{m}}\left(\frac{\bar{R}_m}{Dr_2}\right)^l P_l\left[\sin(\phi_{sc})\right]\right\} \\ & + \frac{\mu}{r_2}\left\{\sum_{l=2}^{\infty}\sum_{m=1}^{l}\left(\frac{\bar{R}_m}{Dr_2}\right)^l P_{l,m}\left[\sin(\phi_{\mathrm{sc}})\right]\left[C_{l,m}\cos(m\lambda_{\mathrm{sc}}) + S_{l,m}\cos(m\lambda_{\mathrm{sc}})\right]\right\} \end{aligned} \tag{20}$$

$$\mu = \frac{m_2}{m_1 + m_2} \tag{21}$$

Because $\dot{u}^2 D^3 \neq G(m_1 + m_2)$, cancellation results in a coefficient function $c$ depending on $f$, expressed as,

$$c(f) = c_1^3 c_2^2 \tag{22}$$

The remaining coefficients $k_1$ and $k_2$ also depend on $f$, expressed as,

$$k_1(f) = \frac{2D'}{D} + \frac{\ddot{f}}{\dot{u}^2} = \frac{2e\sin f}{1+e\cos f} f'\,(1-f') \tag{23}$$

$$k_2(f) = \frac{D''}{D} + \frac{D'\ddot{f}}{D\dot{u}^2} = \frac{e\cos f}{1+e\cos f} f'^2 \tag{24}$$

since according to Eq. (10) and (15)

$$\frac{\ddot{f}}{\dot{u}^2} = -\frac{2e\sin f}{1+e\cos f}\frac{\dot{f}^2}{\dot{u}^2} = -\frac{2e\sin f}{1+e\cos f} f'^2 \tag{25}$$

$$D' = D\frac{e\sin f}{1+e\cos f} f' \tag{26}$$

$$D'' = D\frac{e(\cos f + e + e\sin^2 f)}{(1+e\cos f)^2} f'^2 + D\frac{e\sin f}{1+e\cos f} f'' \tag{27}$$

where

$$f''(f) = \frac{\dot{\omega}\ddot{f}}{\dot{u}^3} = \left(1-\frac{\dot{f}}{\dot{u}}\right)\frac{\ddot{f}}{\dot{u}^2} = -\frac{2e\sin f}{1+e\cos f}\,(1-f')\,f'^2 \tag{28}$$

Elapsed time can also be obtained by integrating,

$$t' = \frac{dt}{du} = \frac{1}{\dot{u}} \tag{29}$$

Equations (16)-(19) represent the restricted three-body problem perturbed by the $J_2$ term of the planet and accommodating the non-spherical terms of the moon. This model is termed “J2-ER3BP+GH” for simplicity, where "-" indicates the perturbation from the planet’s $J_2$ on the primary orbit and "+" indicates the straightforward addition of the moon’s non-spherical influence on the spacecraft’s orbit without perturbing the primary orbit. The J2-ER3BP+GH is believed to be a close approximation of the realistic dynamic model. Bounded orbits from this model are supposed to stay bounded in the real world for the long term given no operational errors.

When $A_2 = 0$, the model becomes the ER3BP plus the moon’s GH terms, termed “ER3BP+GH”, where

$$c(f) = 1+e\cos f \qquad k_1 = 0 \qquad k_2(f) = \frac{e\cos f}{1+e\cos f} \tag{30}$$

When $e = 0$, the system becomes the $J_2$-perturbed circular problem termed “J2-CR3BP+GH”, where

$$c(A_2) = \left(1-\frac{A_2}{a^2}\right)^3\left(1+\frac{2A_2}{a^2}\right)^2 \qquad k_1 = 0 \qquad k_2 = 0 \tag{31}$$

The equations of motion of this autonomous system can be simply written as,

$$x'' - 2y' = \frac{\partial \Omega}{\partial x} \qquad y'' + 2x' = \frac{\partial \Omega}{\partial y} \qquad z'' = \frac{\partial \Omega}{\partial z} \tag{32}$$

where the pseudo-potential $\Omega$ is expressed as,

$$\Omega = \frac{1}{2}(x^2 + y^2) + \frac{1}{c}\left[U + (1-\mu)\left(1 + \frac{A_2}{a^2}\right)x\right] \tag{33}$$

The $J_2$-perturbed circular problem admits a *Jacobi* constant expressed as,

$$C = \frac{1}{2}(x' + y' + z')^2 - \Omega \tag{34}$$

Additionally, if only zonal terms of the moon are considered, meaning the last term of Eq.( 20) is dropped, the model also exhibits symmetries about the $x$-axis and $x$-$z$ plane like the CR3BP. This model is termed "J2-CR3BP+JM". The established method to identify periodic orbits in the CR3BP based on the symmetries can thus be extended to the J2-CR3BP+JM.

## IV. Generation of bounded orbits

To perform bounded motion around the small moon, periodic orbits (PO) can be first identified in the symmetrical J2-CR3BP+JM. There have been many works on the computation of PO and resonant PO families based on the symmetry of the circular problem and bifurcation, using differential correction and pseudo-arclength continuation [19, 28–30]. The PO computed in the J2-CR3BP-JM can serve as the initial guess of the PO in the slightly different but more accurate J2-CR3BP+GH. Multiple shooting can be used to smoothly fit the PO to a slightly different model, as demonstrated in Ref. [11]. Therefore, the PO in the J2-CR3BP+GH can be obtained in the same way.

The next step is to find bounded orbits in the J2-ER3BP+GH. However, POs do not exist in the elliptic problem except for the orbits whose period is resonant with the period of the primary orbit. The quasi-periodic orbit (QPO) is an option for a bounded motion. Similarly, the state of a PO from the J2-CR3BP+GH can serve as the initial guess of QPO. The QPO can be regarded as a trajectory lying on the center manifold associated with $e$, whose initial phase depends on $f_0$ of the primary system. Eccentricity $e$ can be treated as a variable limited to a small value that perturbs the initial condition of a periodic orbit. We can add a new state $\xi = e\cos f$, which combines the two factors, and its derivative $\xi' = -e\sin f \cdot f'$, to the system [31]. The differential equation for the new states is expressed as,

$$\xi'' = (-e\sin f \cdot f')' = -e\cos f \cdot f' - e\sin f \cdot f'' \tag{35}$$

Expressions of $f'$ and $f''$ have been provided in Eqs. (16) and (28). Moreover, $\xi$ and $\xi'$ explicitly determine $e$ and $f$; namely, $g^{-1} : \{\xi, \xi'\} \mapsto \{e, f\}$. Variables $D$, $c$, $f'$, $k_1$, $k_2$ in Eqs. (17)-(19) and $\xi''$ that depend on $e$ and $f$ can be represented as functions of $\xi$ and $\xi'$:

$$D = D(e, f) = D(\xi, \xi') \tag{36}$$

$$f' = f'(e, \xi) = f'(\xi, \xi') \tag{37}$$

$$k_1 = k_1(e, f, f') = k_1(\xi, \xi') \tag{38}$$

$$k_2 = k_2(e, f, f') = k_1(\xi, \xi') \tag{39}$$

$$c = c(e, f) = c(\xi, \xi') \tag{40}$$

$$f'' = f''(e, f) = f''(\xi, \xi') \tag{41}$$

$$\xi'' = \xi''(e, f, f'') = \xi''(\xi, \xi') \tag{42}$$

As a result, Eqs. (17)-(19), and (35) represent an 8-dimensional autonomous system described by the extended states $\boldsymbol{E} = [x, x', y, y', z, z', \xi, \xi']$. The autonomous system allows for easy derivation of the center manifold around a PO, where the QPO lies. To see the eigenstructure of the extended system, the partial derivatives known as the Jacobian matrix at the periodic solution $\bar{\boldsymbol{E}}$ can be expressed as,

$$\mathbf{F}(u) = \frac{\partial \boldsymbol{f}}{\partial \boldsymbol{E}}|_{\bar{\boldsymbol{E}}} = \left[\begin{array}{c|c} \mathbf{A}^{(6\times6)} & \mathbf{B} \\ \hline \mathbf{0} & \mathbf{C}^{(2\times2)} \end{array}\right] \tag{43}$$

where $\mathbf{A}$ represents the Jacobian of the 6-dimensional autonomous circular problem J2-CR3BP+GH, $\mathbf{B}$ represents partial derivatives of velocity and acceleration with respect to the introduced new states $[\xi, \xi']$, and $\mathbf{C}$ represents the Jacobian of the introduced autonomous system at $e = 0$, whose value is,

$$\mathbf{C} = \begin{bmatrix} 0 & 1 \\ -1 & 0 \end{bmatrix} \tag{44}$$

since

$$\frac{\partial \xi''}{\partial \xi}|_{e=0} = -f'|_{e=0} = -1 \qquad \frac{\partial \xi''}{\partial \xi'}|_{e=0} = \frac{f''}{f'}|_{e=0} = 0 \tag{45}$$

The state transition matrix (STM) maps the initial state to the current state, expressed as,

$$\boldsymbol{\Phi} = \frac{\partial \boldsymbol{E}(u)}{\partial \boldsymbol{E}(0)} \tag{46}$$

The initial $\boldsymbol{\Phi}(0) = \mathbf{I}^{(8\times8)}$. The STM can be divided into submatrices corresponding to the structure of the Jacobian matrix in Eq. (43), expressed as,

$$\boldsymbol{\Phi} = \begin{bmatrix} \boldsymbol{\Phi}_{\mathrm{xx}}^{(6\times6)} & \boldsymbol{\Phi}_{\mathrm{x}\xi}^{(6\times2)} \\ \mathbf{0}^{(2\times6)} & \boldsymbol{\Phi}_{\xi\xi}^{(2\times2)} \end{bmatrix} \tag{47}$$

The variations of the divided STMs with respect to $u$ are expressed as,

$$\boldsymbol{\Phi}'_{\mathrm{xx}} = \mathbf{A}\boldsymbol{\Phi}_{\mathrm{xx}} \qquad \boldsymbol{\Phi}'_{\mathrm{x}\xi} = \mathbf{A}\boldsymbol{\Phi}_{\mathrm{x}\xi} + \mathbf{B}\boldsymbol{\Phi}_{\xi\xi} \qquad \boldsymbol{\Phi}'_{\xi\xi} = \mathbf{C}\boldsymbol{\Phi}_{\xi\xi} \tag{48}$$

The Jacobian matrix $\mathbf{A}$ consists of the Jacobian of the CR3BP, whose expression is available in Ref.[28], and the Jacobian associated with the gravity harmonics terms, whose expression is available in Ref.[32]. Therefore, $\boldsymbol{\Phi}_{\mathrm{xx}}$ and $\boldsymbol{\Phi}_{\xi\xi}$ can be obtained by integration. Given the difficulty of deriving analytical expressions for $\mathbf{B}$, $\boldsymbol{\Phi}_{\mathrm{x}\xi}$ can be obtained using finite differencing. The monodromy matrix is $\boldsymbol{\Phi}$ of a periodic orbit after one period. Based on the block structure of $\boldsymbol{\Phi}$, the eigenvectors of the monodromy matrix can be described by

$$\boldsymbol{v}_i = \begin{bmatrix} | \\ \boldsymbol{v}_i^{\text{J2-CR3BP+GH}} \\ | \\ \hline 0 \\ 0 \end{bmatrix}^{\mathrm{T}} \quad (i = 1, \cdots, 6), \quad \boldsymbol{v}_i = \begin{bmatrix} v_{i,1} \\ \vdots \\ \vdots \\ \vdots \\ v_{i,8} \end{bmatrix}^{\mathrm{T}} \quad (i = 7, 8)$$

where $\boldsymbol{v}_i^{\text{J2-CR3BP+GH}}$ $(i = 1, \cdots, 6)$ denotes an eigenvector of the monodromy matrix in the 6-dimensional J2-CR3BP+GH (i.e., $\boldsymbol{\Phi}_{\mathrm{xx}}$ after a period), and $\boldsymbol{v}_i$ $(i = 7, 8)$ denotes the eigenvector associated with $\xi$ and $\xi'$. Thus, given $e$ and initial $f_0$ as well as perturbation on $\xi$ and $\xi'$ components, the corresponding quasi-periodic condition can be generated by adding the displacement vector $\Delta\boldsymbol{E}$ in the span $\{\boldsymbol{v}_7, \boldsymbol{v}_8\}$ to the periodic condition.

Because $\boldsymbol{v}_7$ and $\boldsymbol{v}_8$ generally contain conjugate complex numbers, to cancel imaginary parts, a pair of auxiliary eigenvectors are defined as

$$\boldsymbol{v}_{\mathrm{s}} = \frac{1}{2}(\boldsymbol{v}_7 + \boldsymbol{v}_8) \qquad \boldsymbol{v}_{\mathrm{d}} = \frac{1}{2i}(\boldsymbol{v}_7 - \boldsymbol{v}_8) \tag{49}$$

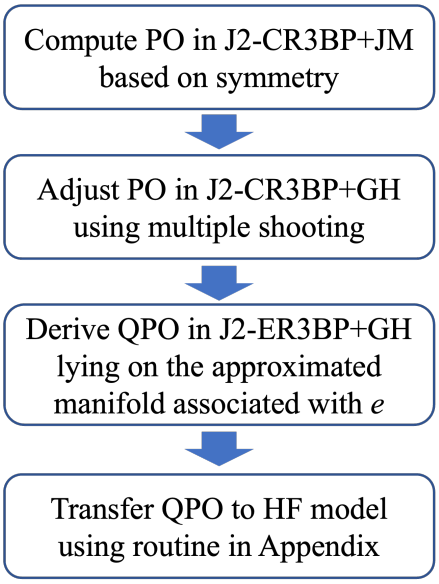


**Fig. 6 Steps to generate bounded orbits.**

Supposing $\boldsymbol{\nu}_\mathrm{s}$ contains $\xi$ component and $\boldsymbol{\nu}_\mathrm{d}$ contains $\xi'$ component, the displacement vector $\Delta\boldsymbol{E}(0)$ is given by,

$$\Delta\boldsymbol{E}(0) = \xi_0/\nu_{\mathrm{s},7} \cdot \boldsymbol{\nu}_\mathrm{s} + \xi_0'/\nu_{\mathrm{d},8} \cdot \boldsymbol{\nu}_\mathrm{d} \tag{50}$$

For the reverse situation,

$$\Delta\boldsymbol{E}(0) = \xi_0/\nu_{\mathrm{d},7} \cdot \boldsymbol{\nu}_\mathrm{d} + \xi_0'/\nu_{\mathrm{s},8} \cdot \boldsymbol{\nu}_\mathrm{s} \tag{51}$$

Because this approach is based on linearization assuming a small $e$, the obtained initial condition for QPO is an approximation to the QPO lying on the center manifold rigorously defined [33–36].

Regarding the generation of bounded orbits in the HF full-ephemeris model, $e$ and $f_0$ at the initial epoch can be resolved from the ephemeris of the primaries, based on which the initial condition of the baseline quasi-periodic orbit in the substitute model J2-ER3BP+GH can be determined. The initial condition can then be converted to an initial state in the HF model using the routine presented in Appendix. Assuming that the substitute model reflects the realistic dynamical environment, the converted initial condition will propagate into a trajectory revolving around the baseline orbit for a long term in the HF model. Steps to produce bounded orbits can be summarized by the flow chart in Fig. 6.

## V. Results

### A. Application to Phobos exploration

Regarding the Mars-Phobos system, Mars' reference radius is 3396 km and $J_2$ is 0.00196, the inclination of their orbit, 1.07°, is small and ignored in the J2-ER3BP+GH, and the osculating eccentricity slightly varies around the mean

eccentricity of 0.015. Based on Kozai's description (i.e., Eq. (7)), the osculating $a$ and mean $\bar{a}$ are 9378 km and 9374.4 km, respectively. Given the close distance to Mars and relatively low gravity, Phobos has a small sphere of influence (SoI) below its surface and the Hill's sphere reaching just 4 km above its surface.

Figure 7 shows the family of near-planar periodic QSO around Phobos in the J2-CR3BP+GH and the associated QPO propagated for 30 days in the J2-ER3BP+GH with $f_0 = -25°$. Note that while POs can be perfectly planar in the J2-CR3BP+JM with only zonal terms, some adjustments on the POs in the out-of-plane direction appear to account for the tesseral and sectional terms in the J2-CR3BP+GH. In Fig. 7, the baseline POs are covered by the span of QPOs. As seen in the close-up figure, the QPO closely revolves around the baseline QSO. Figure 8 presents the envelope of the QPOs starting at various $f_0$ for the QSO of a dimension of $24 \times 48 \times 18$ [km] (i.e., $A_x \times A_y \times A_z$), which belongs to the 3-dimensional 4:5 resonant family.

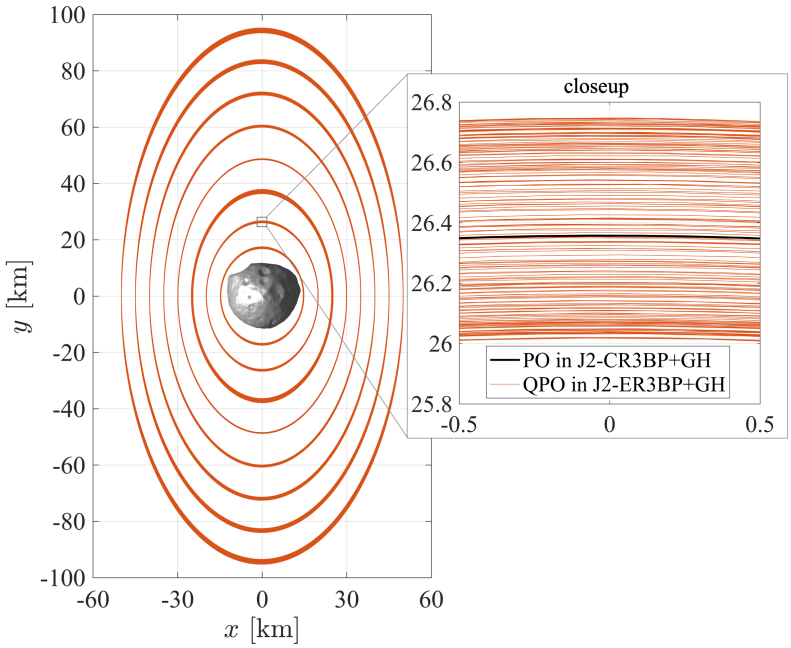


**Fig. 7 Near-planar periodic QSOs around Phobos in the Mar's $J_2$-perturbed circular problem and corresponding QPOs in the elliptic problem.**

**Table 1 Specifications of different dynamic models for Phobos orbiting**

| Dynamic model | J2-ER3BP+GH | ER3BP+GH | HF model |
|---|---|---|---|
| Gravity models | Mars: $2 \times 0$;<br>Phobos: $4 \times 4$ | Mars: point-mass;<br>Phobos: $4 \times 4$ | Sun: point-mass;<br>Mars: $10 \times 10$;<br>Phobos: $4 \times 4$ |
| Ephemeris | $J_2$-perturbed elliptic | elliptic | `mar097` |
| Orientation | coplanar & tidal locked | coplanar & tidal locked | `pck00010` |

The J2-ER3BP+GH is a substitute model whose validity should be examined. It is also desirable to know whether the $J_2$ perturbation should be particularly considered or whether the ER3BP plus moon's gravity model, ER3BP+GH, is

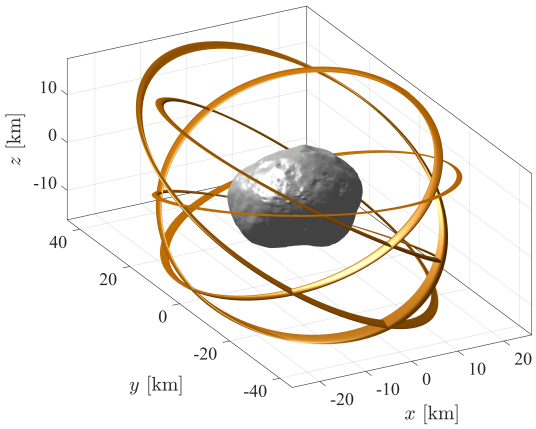


**Fig. 8 Envelop of the QPOs associated with a 3DQSO around Phobos.**

sufficient. Table 1 lists details of the dynamic models selected for comparison and evaluation. The used full Martian spherical harmonics gravity model is truncated at the 10th degree and order, whose values are available from the `jgmro_110b` model [37] developed by JPL. The used full Phobos model is truncated at the 4th degree and order, whose values were provided by the CNES Geodesy group based on Gaskell's Phobos shape model [38]. Higher-degree terms do not significantly affect the QSO more than 10 km above the surface of Phobos. The HF model considers ephemeris and gravity models of the Sun, Mars, and Phobos, where the ephemeris and orientation of the celestial bodies are obtained from the kernel files `mar097` and `pck00010`[39] developed by JPL.

In the examples of comparison, the initial epochs of the HF model are arbitrarily selected to be 2026-02-15 12:00 and 2026-03-15 12:00 UTC, where $f_0$ of the primary orbit are $-125°$ and $150°$, respectively, and the $29 \times 46$ [km] QSO is selected to be the baseline orbit. The orbit evolution for 5 days in different models is shown in Fig. 9 and Fig. 10. The closeup of Fig.9b displays an evident deviation of the HF trajectory from its baseline QPO obtained in the ER3BP+GH for $f_0 = 150°$. The deviation is larger for the situation with $f_0 = -125°$. Figure 10b shows that the HF trajectory closely coincides with the baseline QPO accounting for the $J_2$ term of Mars. This difference highlights the necessity of considering the perturbation from Mars' oblateness. Figure 10 also implies that designed orbits from the J2-ER3BP+GH can sustain for a long time in the realistic dynamical environment without stationkeeping $\Delta v$, provided no operational errors. Compared to the situation resulting from the CR3BP, which is shown in Fig. 1, the dynamical perturbation on the baseline orbits has been significantly reduced. The difficulty of maintaining the baseline orbit in a realistic environment should be minimized accordingly.

*1. Stationkeeping*

Table 2 presents the operational environment for stationkeeping: the ground-based OD errors in the RTN coordinate frame and the control interval, according to the MMX project team [10]. Given the OD errors, control interval

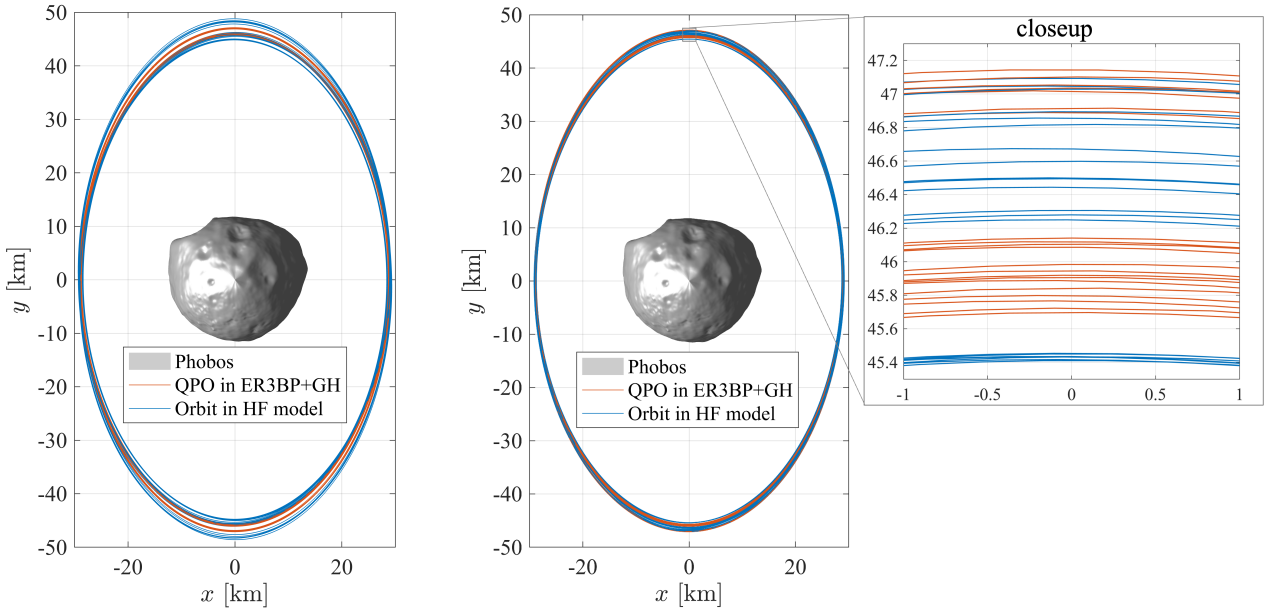


(a) $f_0 = -125°$ (b) $f_0 = 150°$

**Fig. 9 Quasi-periodic QSO obtained in the ER3BP+GH and its evolution in the high-fidelity model.**

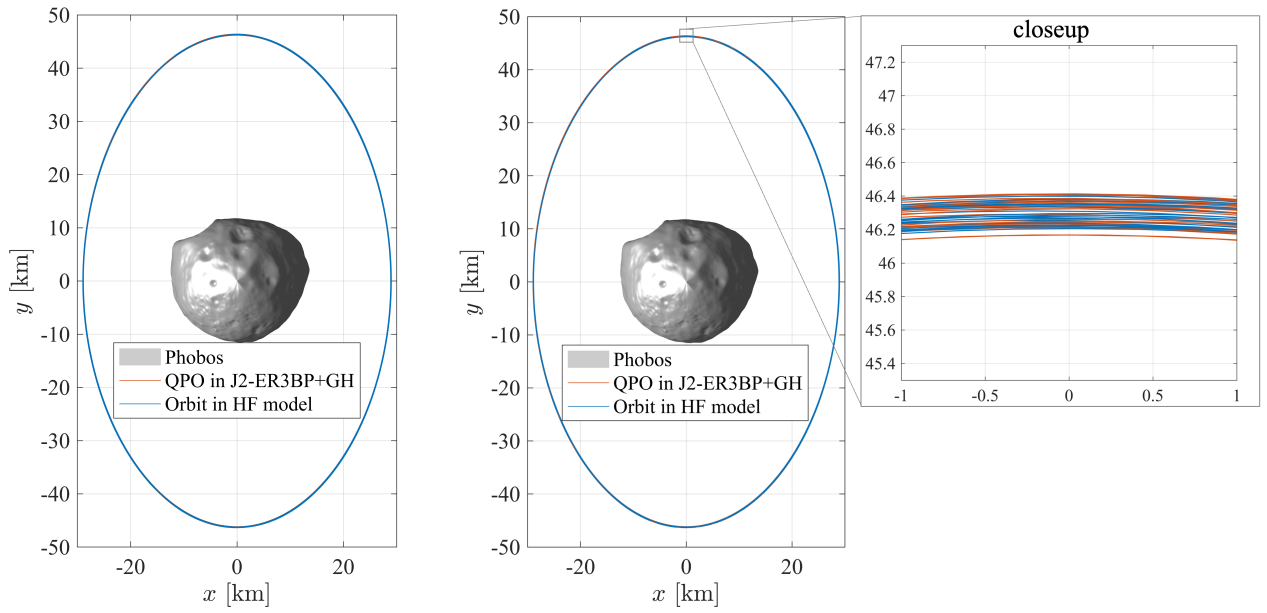


(a) $f_0 = -125°$ (b) $f_0 = 150°$

**Fig. 10 Quasi-periodic QSO obtained in the J2-ER3BP+GH and its evolution in the high-fidelity model.**

**Table 2 Operational environment for stationkeeping around Phobos [10]**

| Condition | Value |
|---|---|
| $1\sigma(\Delta R)$ | 20 m |
| $1\sigma(\Delta T)$ | 175 m |
| $1\sigma(\Delta N)$ | 4 m |
| $1\sigma(\Delta V_R)$ | 53 mm/s |
| $1\sigma(\Delta V_T)$ | 6 mm/s |
| $1\sigma(\Delta V_N)$ | 1 mm/s |
| Control interval | $>$ 5 days |

constraint, and the limited stability domain of QSO, the stationkeeping operation is a challenging task. The baseline orbit should enjoy sufficient effective stability. Therefore, the baseline QPO is obtained in the substitute model sufficiently considering the dynamical perturbation, namely, the J2-ER3BP+GH.

**Table 3 Examined representative QSO**

| QSO dimension | Maximum latitude | Referred to as |
|---|---|---|
| $20 \times 27$ [km] | 0 | QSO-Lc |
| $30 \times 49$ [km] | 0 | unstable QSO |
| $31 \times 51$ [km] | 0 | WS QSO |
| $24 \times 48 \times 18$[km] | 36.9° | 3DQSO-L37 |
| $28.5 \times 50 \times 21.5$ [km] | 37° | 3DQSO-M37 |
| $29 \times 50 \times 20$ [km] | 34.6° | 3DQSO-M35 |

It is desirable to orbit closely around the target, even near an instability region. Additionally, orbits of certain latitudes can facilitate global mapping and landing in the polar regions. The stationkeeping performance is examined over representative low-altitude planar QSO and 3DQSO. The QSOs to be examined are summarized in Table 3. One is the $20 \times 27$ [km] QSO, which is a very low baseline orbit referred to as the "QSO-Lc" in the MMX mission. One is the $30 \times 49$ [km] QSO, which intersects with the unstable period-3 family in the J2-CR3BP+GH and is referred to as the "unstable QSO". The slightly away $31 \times 51$ [km] QSO is considered weakly stable and referred to as the "WS QSO". The selected $24 \times 48 \times 18$ [km] 3DQSO, which is from the 4:5 family, has a low altitude and a maximum geocentric latitude of 36.9° and is referred to as the "3DQSO-L37". The slightly farther $28.5 \times 50 \times 21.5$ [km] 3DQSO, which is from the 6:7 family, has a maximum latitude of 37° and is referred to as the "3DQSO-M37". The less inclined $29 \times 50 \times 20$ [km] 3DQSO, which is from the same 6:7 family, has a maximum latitude of 34.6° and is referred to as the "3DQSO-M35".

**Table 4 Summary of Monte-Carlo simulations of stationkeeping in the high-fidelity model**

| QSO types | Success rate | Average $\Delta v$/time [cm/s] | $1\sigma(\Delta v/\text{time})$ [cm/s] | $\Delta v/5$ days [cm/s] |
|---|---|---|---|---|
| QSO-Lc | 100% | 9.2 | 8.4 | 9.1 |
| Unstable QSO | 84% | 7.6 | 5.6 | 7.6 |
| WS QSO | 100% | 8.8 | 6.1 | 8.6 |
| 3DQSO-L37 | 94% | 19.5 | 17.4 | 18.1 |
| 3DQSO-M37 | 98% | 40.7 | 30.0 | 38.6 |
| 3DQSO-M35 | 100% | 35.4 | 22.5 | 33.7 |

The stationkeeping adopts a straightforward target-point method. At the epoch that an impulsive $\Delta v$ is performed, the initial condition of the baseline QPO is computed for the then phase $f$ of the primary orbit. The initial state is propagated into a baseline trajectory until the next control epoch. The three $\Delta \boldsymbol{v}$ components are solved to minimize distances between the baseline trajectory converted in the HF model and the truth trajectory propagated in the HF model at a series of phases along the orbit (i.e., the targeted points), in a weighted least-square sense. Orbit determination errors are effective at control epochs, influencing the judgment and outcome of the control $\Delta \boldsymbol{v}$. The next $\Delta v$ is performed at a point after 5 days when the propagated state is closest to the nominal initial condition. To compute $\Delta \boldsymbol{v}$ quickly and robustly, the STM is integrated along with the orbit. To be specific, $\Delta \boldsymbol{v}$ is adjusted using the gradient-based differential correction method, where the gradient is derived from the STM. In addition, for a very stable QSO like the QSO-Lc that can tolerate certain deviations without divergence, the control $\Delta v$ is not always applied. $\Delta v$ is performed only if the total residuals exceed a threshold. The threshold and weights of the residuals at the target points are determined via trial and error. For the unstable QSO and the 3DQSO, the threshold is two orders smaller than that of the QSO-Lc.

For each examined QSO, 100 Monte Carlo runs of stationkeeping for 30 consecutive controls in the HF model are performed. The simulations start at 2026-02-01 12:00 UTC, where $f_0 = -83°$. The simulated timeline is longer than 150 days, long enough to tell whether the orbiting operation is robust. The statistical result is summarized in Table 4. The stationkeeping cost generally increases with $A_x$ and $A_z$, which is consistent with the velocity trend of the QSOs. Although dynamical perturbation is minimized, due to the intrinsic QSO instability property and disturbance from OD errors, safe orbiting on the unstable QSO, which intersects with the unstable 3:1 resonance, 3DQSO-L37, and 3DQSO-M37, which are close to the upper instability region (see Fig. 2), cannot be ensured. Nevertheless, robust orbiting is achieved for low-altitude QSO, weakly-stable QSO, and 3DQSO with a latitude up to 35°, a result previously deemed impossible in realistic setups. The stationkeeping cost is also much smaller than that of previous trials verified in the HF model [19, 40]. The stationkeeping costs of 0.5 m/s per month for the planar QSO and 2 m/s per month for the 3DQSO are considered acceptable. Figure 11 shows examples of the maintained orbit legs for the three baseline QSOs that can be robustly maintained. The high-fidelity stationkeeping simulations confirm the effective stability of the baseline orbits and the validity of the J2-ER3BP+GH.

**B. Application to Dimorphos exploration**

Information on the gravity models and ephemerides of the Didymos system to date is of limited accuracy. To represent a possible Didymos-Dimorphos dynamical environment, their trajectories and gravity models are generated based on their orbit and shape parameters from recent observation and the DART's experiment [41–43]. The presumed parameters are listed in Table 5. Dimorphos is considered perfectly tidally locked with its principal axis always pointing to the center of Didymos. Based on the point mass model, the theoretical SoI of Dimorphos extends to 160 km from its center, or 80 km from its surface. Given the tri-axial ellipsoid shape parameters, the gravity harmonics terms $J_2$,

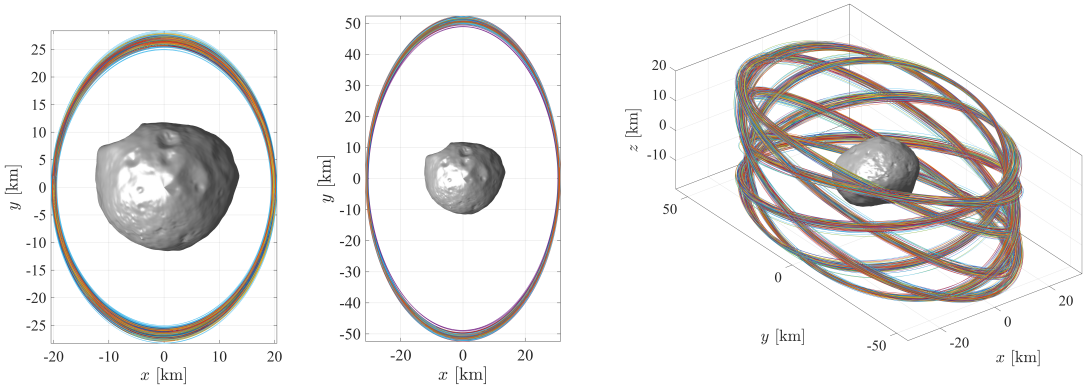


(a) QSO-Lc (b) WS QSO (c) 3DQSO-M35

**Fig. 11 Examples of the maintained QSO legs in the high-fidelity model.**

**Table 5 Presumed parameters of the Didymos-Dimorphos system**

| Parameter | Value |
|---|---|
| Didymos major axis, [m] | 851 |
| Didymos intermediate axis, [m] | 849 |
| Didymos minor axis, [m] | 620 |
| Diameter of volume-equivalent sphere for Didymos, [m] | 761 |
| Sidereal period of Didymos' spin, [h] | 2.26 |
| Dimorphos major axis, [m] | 177 |
| Dimorphos intermediate axis, [m] | 174 |
| Dimorphos minor axis, [m] | 116 |
| Diameter of volume-equivalent sphere for Dimorphos, [m] | 151 |
| Density of Didymos system, [kg/m$^3$] | 2400 |
| Osculating semi-major axis of the binary orbit at $f = 0$, [m] | 1200 |
| Osculating eccentricity at $f = 0$ | 0.044 |

$C_{22}$, $J_4$, $C_{42}$, and $C_{44}$ of both bodies can be calculated [44]. The rest of the Stroke coefficients are assumed to be zero. Asteroids are usually highly irregular. Here, $J_2$ of Didymos is estimated to be 0.1168, 50 times larger than that of Mars. Ephemerides of Didymos and Dimorphos are obtained by integrating their initial position and velocity based on the osculating elements at $f_0 = 0$ under their non-spherical gravity fields.

**Table 6 Specifications of different dynamic models for Dimorphos orbiting**

| | J2-ER3BP+GH | ER3BP+GH | HF model |
|---|---|---|---|
| Gravity models | Didymos: 2×0;<br>Dimorphos: 4×4 | Didymos: point-mass;<br>Dimorphos: 4×4 | Didymos: 4×4;<br>Dimorphos: 4×4 |
| Ephemeris | $J_2$-perturbed elliptic | elliptic | produced |
| Orientation | coplanar & tidal locked | coplanar & tidal locked | coplanar & tidal locked |

Again, the validity of J2-ER3BP+GH is evaluated and compared with the ER3BP+GH. Table 6 lists details of the dynamic models used for comparison and evaluation. The solar radiation pressure, depending on the surface and mass properties of a particular spacecraft, is not considered in the present work, while it is considered influential on spacecraft orbits in the Didymos system in other research works [5]. Given $f_0 = 0$ and a $116.5 \times 128$ [m] QSO, which is within the SoI of Dimorphos, the orbit evolution for 5 days in different models is shown in Fig. 12. It can be seen that the span of the QPO obtained in the J2-ER3BP+GH is thinner than that in the ER3BP+GH. The ER3BP+GH assumes a primary orbit in the two-body problem, and the conversion to the ephemeris model identifies the eccentricity, which is an osculating one, to be 0.044 at $f_0 = 0$. By contrast, the perturbed J2-ER3BP+GH model regards the primary orbit as a mean $J_2$-perturbed orbit and the mean eccentricity of 0.025 is adopted [27, 45], which results in a smaller span of QPO. The orbits propagated in the high-fidelity model indicate that the J2-ER3BP+GH and the adopted mean eccentricity are closer to reality: the HF trajectory coincides with the QPO obtained in the J2-ER3BP+GH, whereas the HF trajectory evidently deviates from the QPO obtained in the ER3BP+GH. This result reveals the significant influence of the gravity of the planet up to the 2nd degree inside the SoI of Dimporphos.

A comparison between J2-ER3BP+GH and the general restricted three-body problem is presented in Fig. 13. The $137 \times 156$ [m] QSO obtained in the CR3BP and ER3BP diverges quickly in the HF model and can crash on Dimorphos before escaping. The same baseline QSO obtained in the J2-ER3BP+GH maintains its nominal motion in the high-fidelity model. The lower panels present the trajectories of all bodies in the HF model, shown in the inertial frame. The clear precession of Dimorphos' orbit reflects the strong influence of Didymos's oblateness, which also causes a significant variation in osculating eccentricity. Thus, it is necessary to specifically consider the $J_2$ perturbation of Didymos in designing harmonious orbits around Dimorphos as Fig. 13a demonstrates. Last, the 107×128×46 [m] orbit, which is a 6:7 3DQSO, around Dimorphos from the J2-ER3BP+GH in different views is shown in Fig. 14. The figure also shows that the trajectory propagated in the HF model closely coincides with the baseline orbit from J2-ER3BP+GH and maintains the baseline motion for an examined interval of 5 days.

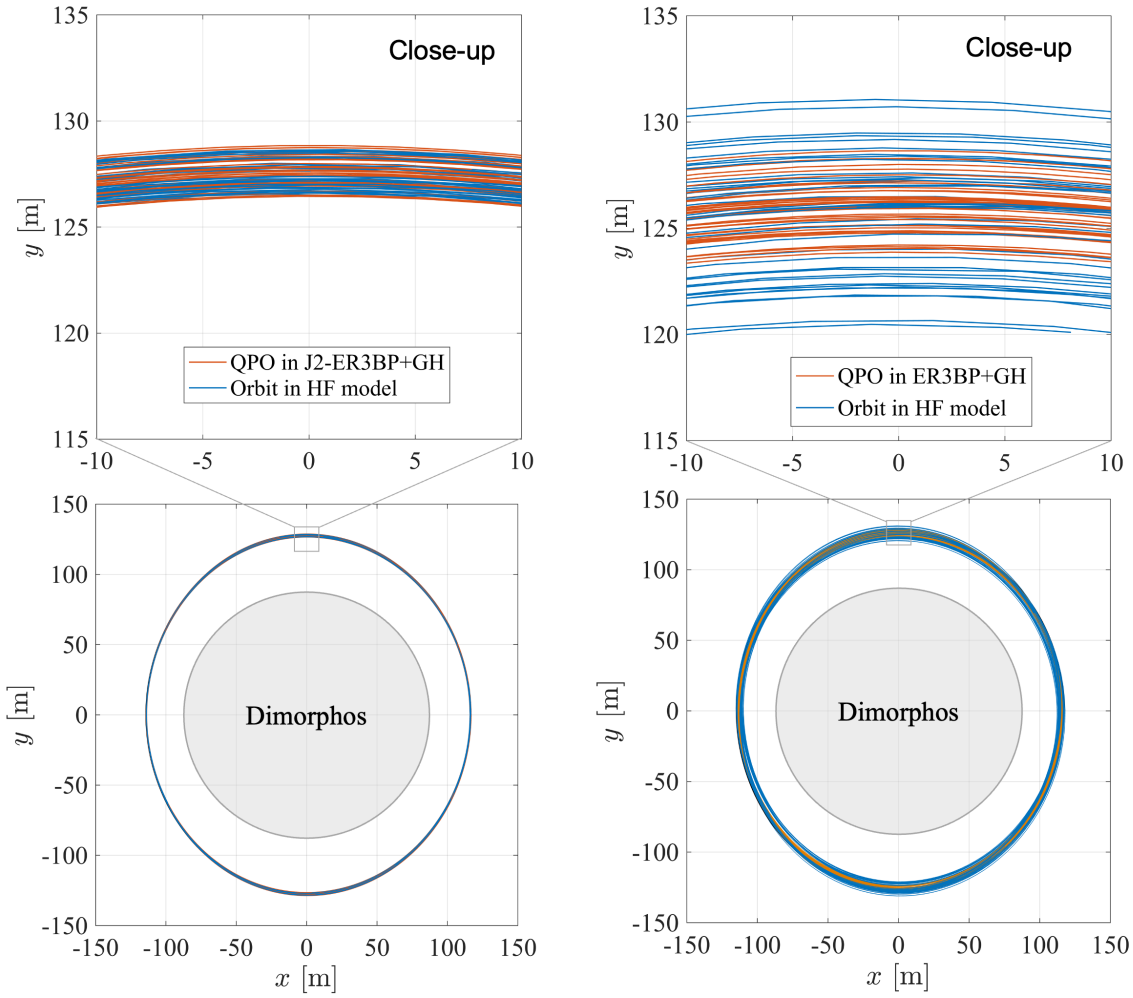


(a) J2-ER3BP+GH vs HF

(b) ER3BP+GH vs HF

**Fig. 12 Model accuracy comparison: 116.5×128 [m] QSO from substitute models and their evolution in the high-fidelity models.**

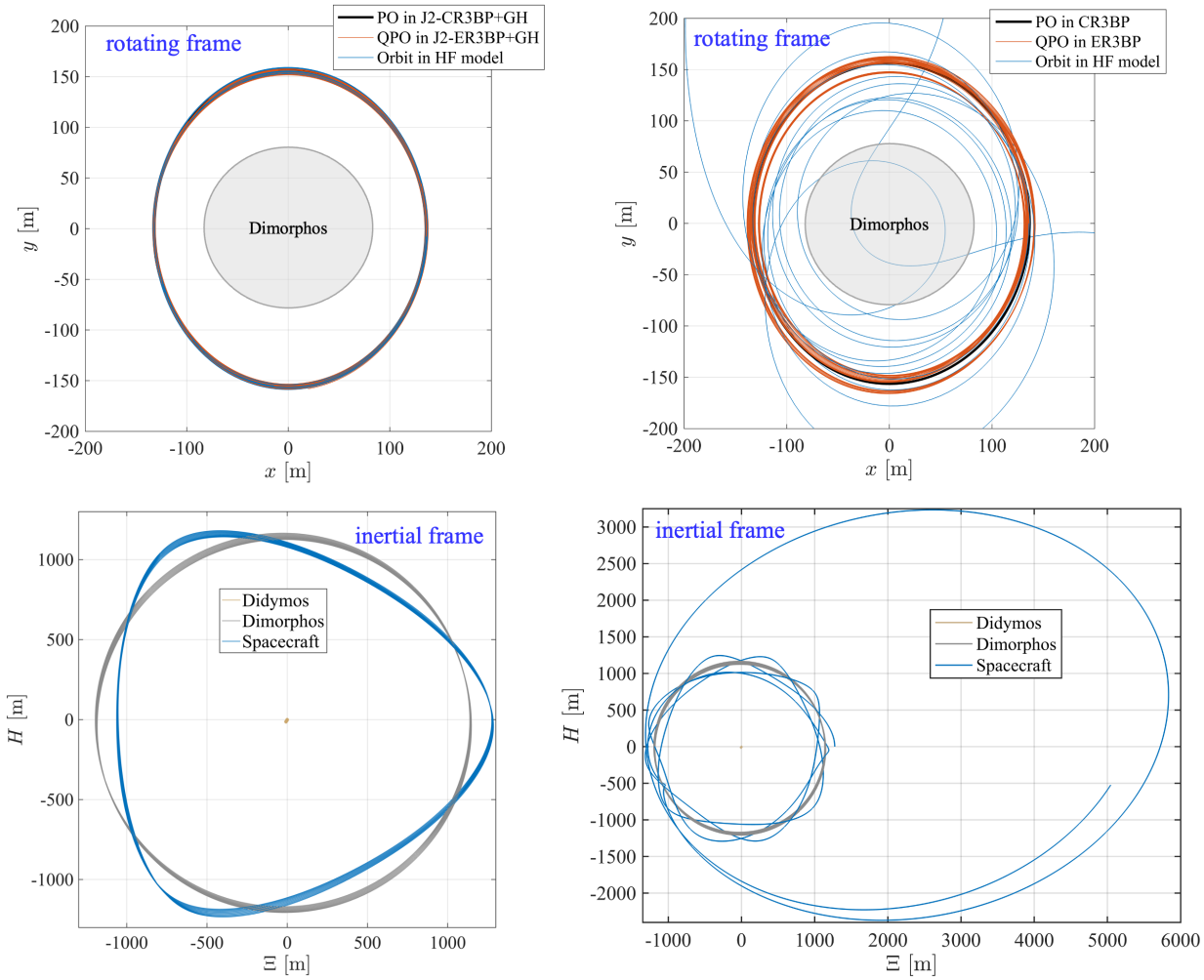


(a) Perturbed restricted 3-body models vs HF

(b) Unperturbed restricted 3-body problems vs HF

**Fig. 13 Model accuracy comparison:** $137 \times 156$ **[m] QSO from substitute models and their evolution in the high-fidelity models for 5 days.**

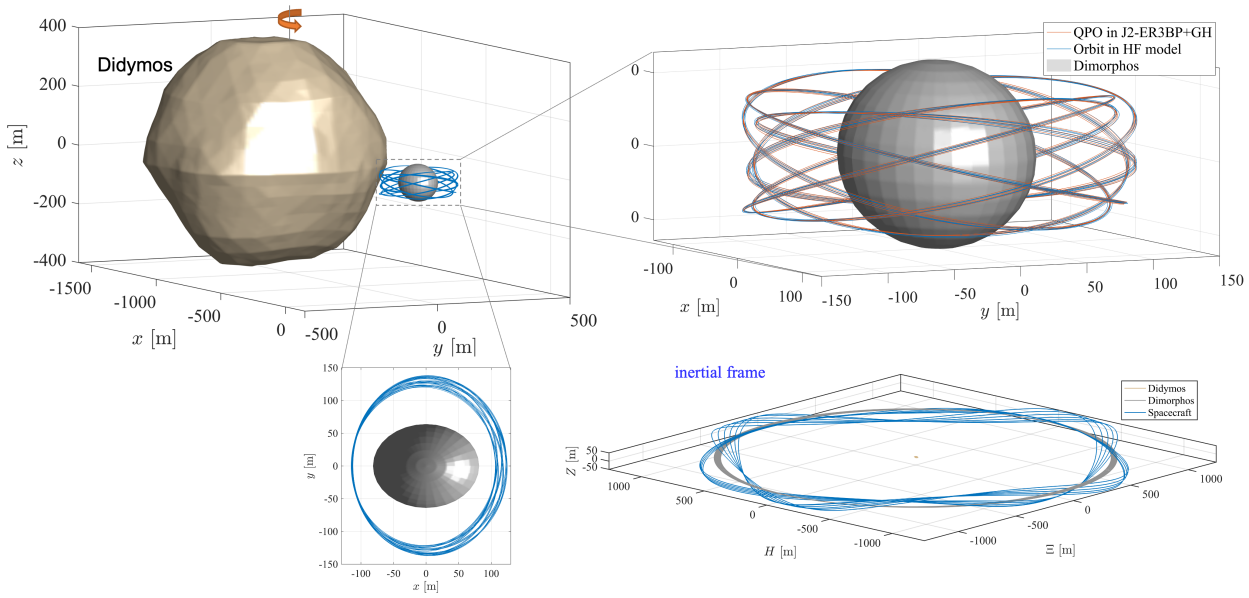


**Fig. 14 A 3DQSO around Didymos from the J2-ER3BP+GH and the corresponding HF trajectory.**

## VI. Conclusion

To support robust proximity orbiting around small moons, such as Martian moons and binary asteroid moons, the present paper develops the "J2-ER3BP+GH" model for revealing enduring bounded orbits. The approach to computing the bounded orbits, periodic and quasi-periodic orbits, was explained. Verification conducted in high-fidelity environments, specifically around Phobos and Dimorphos, demonstrates the efficacy of the J2-ER3BP+GH model in capturing the orbital dynamics near these small moons. In contrast, other substitute models like the CR3BP, ER3BP, and ER3BP+GH prove inadequate for proper baseline orbit design in small-moon explorations, where accounting for the $J_2$ perturbation of the planet is necessary. As the baseline orbits from J2-ER3BP+GH receive small dynamical perturbation, for Phobos exploration, we can achieve robust stationkeeping in the weakly-stable, low-altitude, and mid-latitude (i.e., 35°) regions at acceptably small cost: around 0.5 m/s per month for the planar QSO and 2 m/s per month for the 3-dimensional QSO.

## Appendix: Conversion to the ephemeris model

The steps of conversion from the substitute model to the full-ephemeris model used in this work are the same as those documented in a CNES technical note [46]. The dimensionless position vector from the moon to the spacecraft, $\hat{\boldsymbol{r}}$, is first converted to the dimensional one, $\boldsymbol{r}_{\text{ms}}$, which is expressed as,

$$\boldsymbol{r}_{\text{ms}} = \hat{\boldsymbol{r}} \times LU(t) \tag{52}$$

where the time-dependent length unit $LU(t) = D$ is the norm of the position of the moon relative to the planet, $\left\|\boldsymbol{R}_{\mathrm{pm}}\right\|$, read from the ephemeris. As for the time unit $TU$ and the angular rate $\dot{u}$, the angular momentum $\boldsymbol{h}$ is first computed from,

$$\boldsymbol{h} = \boldsymbol{R}_{\mathrm{pm}} \times \boldsymbol{V}_{\mathrm{pm}} \tag{53}$$

where $\boldsymbol{V}_{\mathrm{pm}}$ is the velocity of the moon relative to the planet. The angular rate of the primary orbit is,

$$\dot{u} = \|\boldsymbol{h}\| / LU^2 \tag{54}$$

The time-dependent time length is computed from,

$$TU(t) = 1/\dot{u} \tag{55}$$

The change rate of $LU$ is computed from,

$$\dot{LU}(t) = \boldsymbol{R}_{\mathrm{pm}} \cdot \boldsymbol{V}_{\mathrm{pm}} / LU \tag{56}$$

The dimensionless velocity, $\hat{\boldsymbol{v}}$, translates to part of the dimensional velocity, $\boldsymbol{v}_{\mathrm{ms}}$, as

$$\boldsymbol{v}_{\mathrm{ms}} = \hat{\boldsymbol{v}} \cdot LU/TU + [0, 0, \dot{u}]^{\mathrm{T}} \times \boldsymbol{r}_{\mathrm{ms}} + \hat{\boldsymbol{r}} \cdot \dot{LU} \tag{57}$$

For rotation from the rotating frame to the inertial frame, unit vectors of the rotating frame are first computed from

$$\boldsymbol{i}_{\mathrm{x}} = \boldsymbol{R}_{\mathrm{pm}} / \left\|\boldsymbol{R}_{\mathrm{pm}}\right\| \tag{58}$$

$$\boldsymbol{i}_{\mathrm{z}} = \boldsymbol{h} / \|\boldsymbol{h}\| \tag{59}$$

$$\boldsymbol{i}_{\mathrm{y}} = \boldsymbol{i}_{\mathrm{z}} \times \boldsymbol{i}_{\mathrm{x}} \tag{60}$$

The rotation matrix from the rotating frame to the inertial frame is expressed as,

$$\mathbf{T} = \begin{bmatrix} \boldsymbol{i}_{\mathrm{x}} & \boldsymbol{i}_{\mathrm{y}} & \boldsymbol{i}_{\mathrm{z}} \end{bmatrix} \tag{61}$$

Finally, the position and velocity of the spacecraft relative to the moon in the inertial frame are computed from,

$$\begin{aligned} \boldsymbol{R}_{\mathrm{ms}} &= \mathbf{T} \cdot \boldsymbol{r}_{\mathrm{ms}} \\ \boldsymbol{V}_{\mathrm{ms}} &= \mathbf{T} \cdot \boldsymbol{v}_{\mathrm{ms}} \end{aligned} \tag{62}$$

## Funding Sources

This work is supported by the JSPS Grant-in-Aid for Early-Career Scientists (No. 22K14424).

## Acknowledgment

The first author wishes to thank Daniel Scheeres, Damennick Henry (CU Boulder), Naoki Hiraiwa (Kyushu Univ.), Hitoshi Ikeda (JAXA), Yue Wang (Beihang), Stefano Carletta (Sapienza) for the inspiring discussions, and Kaito Miyoshi (Kyushu Univ.) for cross-checks of the equations and codes.

## References

[1] Kuramoto, K., Kawakatsu, Y., Fujimoto, M., Araya, A., Barucci, M. A., et al., "Martian moons exploration MMX: sample return mission to Phobos elucidating formation processes of habitable planets," *Earth, Planets and Space*, Vol. 74, No. 1, 2022, p. 12. https://doi.org/10.1186/s40623-021-01545-7.

[2] Kawakatsu, Y., Kuramoto, K., Usui, T., Sugahara, H., Ootake, H., et al., "Preliminary design of Martian Moons eXploration (MMX)," *Acta Astronautica*, Vol. 202, 2023, pp. 715–728. https://doi.org/https://doi.org/10.1016/j.actaastro.2022.09.009.

[3] Michel, P., Küppers, M., Bagatin, A. C., Carry, B., Charnoz, S., et al., "The ESA Hera Mission: Detailed Characterization of the DART Impact Outcome and of the Binary Asteroid (65803) Didymos," *The Planetary Science Journal*, Vol. 3, No. 7, 2022, p. 160. https://doi.org/10.3847/PSJ/ac6f52.

[4] Gil-Fernández, J., Casasco, M., Carnelli, I., Martino, P., and Küppers, M., "HERA autonomous guidance, navigation and control experiments: Enabling Better asteroid science & future missions," *8th European Conference for Aeronautics and Space Sciences (EUCASS), Madrid, Spain*, 2019.

[5] Ferrari, F., Franzese, V., Pugliatti, M., Giordano, C., and Topputo, F., "Trajectory Options for Hera's Milani CubeSat Around (65803) Didymos," *The Journal of the Astronautical Sciences*, Vol. 68, No. 4, 2021, pp. 973–994. https://doi.org/10.1007/s40295-021-00282-z.

[6] Bottiglieri, C., Piccolo, F., Giordano, C., Ferrari, F., and Topputo, F., "Applied Trajectory Design for CubeSat Close-Proximity Operations around Asteroids: The Milani Case," *Aerospace*, Vol. 10, No. 5, 2023. https://doi.org/10.3390/aerospace10050464.

[7] Karatekin, Ö., Le Bras, E., Van wal, S., Herique, A., Tortora, P., et al., "Juventas Cubesat for the Hera mision," *European Planetary Science Congress*, 2021, pp. EPSC2021–750. https://doi.org/10.5194/epsc2021-750.

[8] Chen, H., Rambaux, N., Lainey, V., and Hestroffer, D., "Mothership-Cubesat Radioscience for Phobos Geodesy and Autonomous Navigation," *Remote Sensing*, Vol. 14, No. 7, 2022. https://doi.org/10.3390/rs14071619.

[9] Woodard, M., Cosgrove, D., Morinelli, P., Marchese, J., Owens, B., and Folta, D., "Orbit determination of spacecraft in Earth-Moon L1 and L2 libration point orbits," *Advances in the Astronautical Sciences*, Vol. 142, No. 1, 2012, pp. 1683–1696.

[10] Ikeda, H., Oki, Y., Sakamoto, T., Nakano, M., Nishimura, K., et al., "Flight Dynamics Operation Strategies of Martian Moons eXploration (MMX)," *34th International Symposium on Space Technology and Science*, Kurume, Japan, 2023.

[11] Zamaro, M., and Biggs, J. D., "Natural motion around the Martian moon Phobos: the dynamical substitutes of the Libration Point Orbits in an elliptic three-body problem with gravity harmonics," *Celestial Mechanics and Dynamical Astronomy*, Vol. 122, No. 3, 2015, pp. 263–302. https://doi.org/10.1007/s10569-015-9619-2.

[12] Pushparaj, N., Baresi, N., and Kawakatsu, Y., "Transfers and orbital maintenance of spatial retrograde orbits for Phobos exploration," *Acta Astronautica*, Vol. 189, 2021, pp. 452–464. https://doi.org/https://doi.org/10.1016/j.actaastro.2021.09.008.

[13] SZEBEHELY, V., *Theory of Orbit*, Academic Press, 1967.

[14] Douskos, C. N., and Markellos, V. V., "Out-of-plane equilibrium points in the restricted three-body problem with oblateness," *Astronomy and Astrophysics*, Vol. 446, No. 1, 2006, pp. 357–360. https://doi.org/10.1051/0004-6361:20053828.

[15] Salazar, F., Alkhaja, A., Fantino, E., and Alessi, E. M., "Science orbits in the Saturn–Enceladus circular restricted three-body problem with oblate primaries," *Acta Astronautica*, Vol. 180, 2021, pp. 398–416. https://doi.org/https://doi.org/10.1016/j.actaastro.2020.12.045.

[16] Kozai, Y., "THE MOTION OF A CLOSE EARTH SATELLITE," *The Astronomical Journal*, Vol. 64, 1959, pp. 367–377.

[17] Wiesel, W. E., "Stable Orbits About the Martian Moons," *Journal of Guidance, Control, and Dynamics*, Vol. 16, No. 3, 1993, pp. 434–440. https://doi.org/10.2514/3.21028.

[18] Chen, H., Canalias, E., Hestroffer, D., and Hou, X., "Stability Analysis of Three-dimensional Quasi-satellite Orbits around Phobos," *Proceedings of the 69th International Astronautical Congress*, Bremen, Germnay, 2018.

[19] Chen, H., Canalias, E., Hestroffer, D., and Hou, X., "Effective Stability of Quasi-Satellite Orbits in the Spatial Problem for Phobos Exploration," *Journal of Guidance, Control, and Dynamics*, Vol. 43, No. 12, 2020, pp. 2309–2320. https://doi.org/10.2514/1.G004911.

[20] Hénon, M., "Numerical Exploration of the Restricted Problem. V. Hill's case: Periodic Orbits and Their Stability," *Astronomy and Astrophysics*, 1969, pp. 223–238.

[21] Benest, D., "Effects of the Mass Ratio on the Existence of Retrograde Satellites in the PCR3BP," *Astronomy & Astrophysics*, Vol. 45, 1975, pp. 353–363. https://doi.org/10.1017/CBO9781107415324.004.

[22] Sidorenko, V. V., Neishtadt, A. I., Artemyev, A. V., and Zelenyi, L. M., "Quasi-satellite orbits in the general context of dynamics in the 1:1 mean motion resonance: perturbative treatment," *Celestial Mechanics and Dynamical Astronomy*, Vol. 120, No. 2, 2014, p. 131–162. https://doi.org/10.1007/s10569-014-9565-4.

[23] Lara, M., "On perturbation solutions in the restricted three-body problem dynamics," *Acta Astronautica*, Vol. 195, 2022, pp. 596–604. https://doi.org/https://doi.org/10.1016/j.actaastro.2022.01.022.

[24] Kogan, Y., "Quasi-satellite orbits and their applications," *Dresden International Astronautical Federation Congress*, 1990.

[25] Hénon, M., "Numerical exploration of the restricted problem. VI. Hill's Case: Non-Periodic Orbits," *Astronomy and Astrophysics*, Vol. 9, 1970, pp. 24–36. https://doi.org/10.1017/CBO9781107415324.004.

[26] Lam, T., and Whiffen, G. J., "Exploration of Distant Retrograde Orbits Around Europa," *AAS/AIAA Space Flight Mechanics Meeting*, Copper Mountain, Colorado, USA, 2005.

[27] Vallado, D. A., *Fundamentals of Astrodynamics and Applications*, 5th ed., Microcosm Press and Springer, US, 2022.

[28] Howell, K., "Three-dimensional, periodic, 'halo' orbits," *Celestial mechanics*, Vol. 32, No. 1, 1984, pp. 53–71. https://doi.org/10.1007/BF01358403.

[29] Doedel, E. J., Paffenroth, R. C., Keller, H. B., Dichmann, D. J., Galán-Vioque, J., and Vanderbauwhede, A., "Computation of Periodic Solutions of Conservative Systems with Application to the 3-Body Problem," *International Journal of Bifurcation and Chaos*, Vol. 13, No. 06, 2003, pp. 1353–1381. https://doi.org/10.1142/S0218127403007291.

[30] Lara, M., Russell, R. P., and Villac, B. F., "Classification of the Distant Stability Regions at Europa," *Journal of Guidance, Control, and Dynamics*, Vol. 30, No. 2, 2007, pp. 409–418. https://doi.org/10.2514/1.22372.

[31] Akiyama, Y., Bando, M., and Hokamoto, S., "Extended state space approach for trajectory design in elliptic restricted three-body problem," *Proceedings of the 69th International Astronautical Congress*, Bremen, Germany, 2018.

[32] Montenbruck, O., and Gill, E., *Linearization*, Springer Berlin Heidelberg, Berlin, Heidelberg, 2000, pp. 233–256. https://doi.org/10.1007/978-3-642-58351-3_7.

[33] Gómez, G., and Mondelo, J., "The dynamics around the collinear equilibrium points of the RTBP," *Physica D: Nonlinear Phenomena*, Vol. 157, No. 4, 2001, pp. 283–321. https://doi.org/https://doi.org/10.1016/S0167-2789(01)00312-8.

[34] Olikara, Z. P., and Howell, K. C., "Computation of Quasi-Periodic Invariant Tori in the Restricted Three-Body Problem," *AAS/AIAA Space Flight Mechanics Meeting*, San Diego, USA, 2010.

[35] Olikara, Z. P., and Scheeres, D. J., "NUMERICAL METHOD FOR COMPUTING QUASI-PERIODIC ORBITS AND THEIR STABILITY IN THE RESTRICTED THREE-BODY PROBLEM," *1st International-Academy-of-Astronautics Conference on Dynamics and Control of Space Systems (DyCoSS)*, edited by A. Guerman, P. Bainum, and J. Contant, Univelt Inc., United States, 2012, pp. 911–1507.

[36] Olikara, Z. P., "Computation of quasi-periodic tori and heteroclinic connections in astrodynamics using collocation techniques," Phd thesis, University of Colorado Boulder, 2016.

[37] JPL, "MRO gravity science archive," https://pds-geosciences.wustl.edu/missions/mro/gravity.htm, 2023. Retrieved 11 December 2023.

[38] Gaskell, R., "Gaskell Phobos Shape Model V1.0," Tech. rep., NASA Planetary Data System, 2011.

[39] JPL, "Planetary Data System Navigation Node," https://naif.jpl.nasa.gov/pub/naif/generic_kernels/, 2023. Retrieved 11 December 2023.

[40] Canalias, E., Lorda, L., Chen, H., and Ikeda, H., "TRAJECTORY DESIGN AND OPERATIONAL CHALLENGES FOR THE EXPLORATION OF PHOBOS," *2021 AAS/AIAA Astrodynamics Specialist Conference*, edited by R. Wilson, J. Shan, K. Howell, and F. Hoots, Univelt Inc., 2021, pp. 1493–1507.

[41] Naidu, S., Benner, L., Brozovic, M., Nolan, M., Ostro, S., et al., "Radar observations and a physical model of binary near-Earth asteroid 65803 Didymos, target of the DART mission," *Icarus*, Vol. 348, 2020, p. 113777. https://doi.org/https://doi.org/10.1016/j.icarus.2020.113777.

[42] Daly, R. T., Ernst, C. M., Barnouin, O. S., Chabot, N. L., Rivkin, A. S., et al., "Successful kinetic impact into an asteroid for planetary defence," *Nature*, Vol. 616, No. 7957, 2023, pp. 443–447. https://doi.org/10.1038/s41586-023-05810-5.

[43] Cheng, A. F., Agrusa, H. F., Barbee, B. W., Meyer, A. J., Farnham, T. L., et al., "Momentum transfer from the DART mission kinetic impact on asteroid Dimorphos," *Nature*, Vol. 616, No. 7957, 2023, pp. 457–460. https://doi.org/10.1038/s41586-023-05878-z.

[44] Balmino, G., "Gravitational potential harmonics from the shape of an homogeneous body," *Celestial Mechanics and Dynamical Astronomy*, Vol. 60, No. 3, 1994, pp. 331–364. https://doi.org/10.1007/BF00691901.

[45] Kwok, J. H., "The artificial satellite analysis program (ASAP), version 2.0," Internal Document EM 312/87-153, Jet Propulsion Laboratory, Pasadena, 1987.

[46] Chen, H., "Stability, Stationkeeping, and Application of Three-Dimensional Quasi-Satellite Orbits around Phobos," Tech. rep., CNES, Nov. 2020. DYNVOL-NT-MAN/RTD-1020-CNES.